Astronomical Techniques and Instruments, Vol. 2, September 2025, 280–287

Article Open Access

Optimization of compressed sensing-based radio interferometric imaging: hyperparameter selection

Haoming Dai[1,2], Li Deng[1*]

[1]*State Key Laboratory of Solar Activity and Space Weather*, *National Space Science Center*, *Chinese Academy of Sciences*, *Beijing* 100190, *China*

[2]*University of Chinese Academy of Sciences*, *Beijing* 100190, *China*

*Correspondence: dengli@nssc.ac.cn

Received: January 10, 2025; Accepted: May 6, 2025; Published Online: May 23, 2025; https://doi.org/10.61977/ati2025009; https://cstr.cn/32083.14.ati2025009

Citation: Dai, H. M., Deng, L. 2025. Optimization of compressed sensing-based radio interferometric imaging: hyperparameter selection. *Astronomical Techniques and Instruments*, **2**(5): 280−287. https://doi.org/10.61977/ati2025009.

Abstract: Radio interferometric imaging samples visibility data in the spatial frequency domain and then reconstructs the image. Because of the limited number of antennas, the sampling is usually sparse and noisy. Compressed sensing-based on convex optimization is an effective reconstruction method for sparse sampling conditions. The hyperparameter for the l_1 regularization term is an important parameter that directly affects the quality of the reconstructed image. If its value is too high, the image structure will be missed. If its value is too low, the image will have a low signal-to-noise ratio. The selection of hyperparameters under different levels of image noise is studied in this paper, and solar radio images are used as examples to analyze the optimization results of compressed sensing algorithms under different noise conditions. The simulation results show that when the salt-and-pepper noise density is between 10% and 30%, the compressed sensing algorithm obtains good reconstruction results. Moreover, the optimal hyperparameter value has a linear relationship with the noise density, and the mean squared error of regression is approximately 8.10×10^{-8}.

Keywords: Astronomy image processing; Radio interferometers; Radio telescopes

1. INTRODUCTION

Because of the good linearity of the laws governing salt-and-pepper noise, we believe that some of these laws can be exploited in interferometric imaging. Traditional signal sampling must satisfy the Nyquist sampling theorem to effectively recover the original signal. However, sampling is usually sparse and noisy due to the limited number of antennas. The compressed sensing theory proposed by Candès and Tao in 2006 aims to combine data acquisition with compression[1–3]. Its principle is to use the feature of signal sparsity to enable the efficient reconstruction of sparsely sampled noisy images.

Compressed sensing is also applied in the field of image denoising. Elad and Aharon proposed a dictionary-based denoising method[4] called the K-SVD algorithm. The main drawback of such methods is that they require proximity between the reconstructed denoised image and the original noisy image, which may result in some residual noise in the denoised image. Yang et al. proposed a dictionary learning method[5], using a sparse representation model to construct and represent images. They reformulated the problem as a dictionary learning issue by selecting bases that can be sparsely combined to represent the processed image and achieve the minimum global reconstruction error (e.g., Mean Squared Error (MSE)). Peyr introduced an effective Compressed Sensing (CS) method based on tree-structured dictionaries[6], which uses iterative thresholding methods to recover signals and estimate the best basis. Shahdoosti proposed a block-matching-based algorithm[7] that groups the noisy image using block-matching techniques and then employs the same sparse vector for all blocks within each group.

Bobin et al. applied compressed sensing algorithms to radio interferometric imaging reconstruction[8]. Wenger et al. proposed a simulation of continuous observation of radio astronomical targets using compressed sensing algorithms[9]. In their study, three methods based on compressed sensing, l_1, l_2, and $l_{(0,\infty)}$, were proposed, all of which showed good performance in reconstructing the images of observed dynamic targets. However, they did not consider noise in their analysis.

Iterative Shrinkage/Thresholding Algorithm (ISTA), Fast Iterative Shrinkage/Thresholding Algorithm (FISTA),

and Two-Step Iterative Shrinkage/Thresholding (TwIST) are commonly used optimization algorithms in the field of compressed sensing. ISTA approximates the sparse solution by iteratively applying soft thresholding to update the solution, with a convergence rate of $O(1/k)$. FISTA, proposed by Beck and Teboulle[10], accelerates convergence by introducing momentum in the iteration of ISTA, with a convergence rate of $O(1/k^2)$. TwIST, proposed by Bioucas-Dias and Figueiredo[11], is a two-step iterative shrinkage/thresholding algorithm for image recovery. This method combines gradient descent and soft thresholding operations, thereby improving the convergence speed and stability of the algorithm. All of the above algorithms use the l_1 regularization term for image reconstruction, but lack an analysis of the specific value that this hyperparameter should take. The selection process, which is based on noise density and the optimization of peak signal-to-noise ratio (PSNR) and structural similarity (SSIM), remains an area of ongoing research.

In compressed sensing image reconstruction, the hyperparameter of the l_1 regularization term is an important parameter that directly affects the quality of the reconstructed image. If the parameter value is too high, it may over-regularize to values near zero; if the parameter value is too low, this will cause a low PSNR in the image. Therefore, this study conducted a detailed investigation of the selection of hyperparameter values for the l_1 regularization term in radio interferometric image reconstruction, analyzing which strategies are suitable under different noise conditions.

2. IMAGE RECONSTRUCTION WITH COMPRESSED SENSING

2.1. Interferometric Imaging Principle

According to the principle of interferometric imaging in synthetic aperture radiometers, the original image $I \in \mathbb{R}^{n\times n}$ is related to the visibility function $V \in \mathbb{C}^{n\times n}$, sampled in the spatial frequency domain using the following Fourier transform,

$$V(u,v) = \int_{\mathbb{R}} I(x,y) \mathrm{e}^{-\mathrm{i}(ux+vy)} \mathrm{d}x\mathrm{d}y. \tag{1}$$

Let $\mathcal{F}$ be a mapping from $\mathbb{R}^{n\times n}$ to $\mathbb{C}^{n\times n}$, which maps an $n\times n$ pixel image to an $n\times n$ pixel visibility through Equation (1). Under ideal conditions, this mapping is represented by $\mathcal{F}$, and the discrete Fourier transform can be written in the following form,

$$V = \mathcal{F}(I)\,. \tag{2}$$

Different antenna array distributions have different sampling distributions in the spatial frequency domain. Hence there exists a mask vector $M \in \{0,1\}^{n\times n}$, representing the sampling capability of the antenna array in the spatial frequency domain, defined as follows,

$$M(u,v) = \begin{cases} 1 & (u,v) \text{ is sampled} \\ 0 & (u,v) \text{ is not sampled} \end{cases}. \tag{3}$$

Because of the various factors that cause noise in actual observations, this study focuses on random salt-and-pepper noise, denoted as $N \in \mathbb{R}^{n\times n}$.The final obtained visibility function V can be calculated as follows,

$$V = M \odot \mathcal{F}(I+N), \tag{4}$$

where $\odot$ represents element-wise multiplication, indicating that mask M acts on the visibility across the entire space.

2.2. Compressed Sensing Image Reconstruction Algorithm Design

When the observations of an object have sparse characteristics, the compressed sensing method can effectively perform image reconstruction. The compressed sensing algorithm is a nonlinear regularization optimization algorithm expressed as follows,

$$\min_x \|x\|_0 \text{ s.t. } y = h(x), \tag{5}$$

where $y = h(x)$ is the underdetermined constraint condition for the optimization problem, and $h(x)$ is the optimization constraint, which requires first-order differentiability (Lipschitz continuity) and must be convex. In fact, because of the difficulty of performing calculations related to the l_0-norm while ensuring sparsity, this problem is usually transformed into an l_1-norm optimization problem, which converts it into a convex optimization problem. When the observation matrix satisfies RIP, these two problems are equivalent,

$$\min_x \|x\|_1 \text{ s.t. } y = h(x). \tag{6}$$

To simplify the problem, the problem in Equation (6) can be further transformed into an unconstrained optimization problem. In this step, a hyperparameter γ is introduced to represent the degree of image compression. The new unconstrained optimization problem is formulated as follows,

$$\min_x \frac{1}{2}\|y - h(x)\|_2^2 + \gamma\|x\|_1. \tag{7}$$

The specific case considered in this study, i.e., that the visibility corresponding to the reconstructed image must be equal to the observed visibility, with $y = V$ and $h(x) = M \odot \mathcal{F}(x)$. Thus, the image reconstruction problem is transformed into the following unconstrained optimization problem,

$$\min_x \frac{1}{2}\|V - M \odot \mathcal{F}(x)\|_2^2 + \gamma\|x\|_1. \tag{8}$$

For convenience, the relationship between functions

$f(x)$ and $g(x)$ is given below,

$$f(x)=\frac{1}{2}\|V-M\odot\mathcal{F}(x)\|_2^2,\quad g(x)=\gamma\|x\|_1. \tag{9}$$

For the unconstrained optimization problem that includes the l_1-regularized term $g(x)$, because $g(x)$ is non-differentiable, the FISTA method can be used to solve it[10]. This method requires $f(x)$ to be differentiable and $\nabla f(x)$ to be Lipschitz continuous, but $g(x)$ only needs to have a proximity operator. The optimization problem shown in Equation (8) can be solved using the three-step iterative algorithm given by the three following equations:

$$x_k=p_L(y_k)\ , \tag{10}$$

$$t_{k+1}=\frac{1+\sqrt{1+4t_k^2}}{2}\ , \tag{11}$$

$$y_{k+1}=x_k+\frac{t_k-1}{t_{k+1}}(x_k-x_{k-1}), \tag{12}$$

$$p_L(y)=\underset{x}{\operatorname{argmin}}\left\{\gamma\|x\|_1+\frac{L}{2}\left\|x-\left(y-\frac{1}{L}\nabla f(y)\right)\right\|_2^2\right\}. \tag{13}$$

Here p_L is the proximity operator. L is the Lipschitz constant of $\nabla f(y)$. In this problem, $L=n^2$. The proximity operator shown in Equation (13) is the shrinkage operator in LASSO, which is the following closed-form solution,

$$p_L(y)=\begin{cases}\hat{x}-\dfrac{\gamma}{L} & \hat{x}>\dfrac{\gamma}{L}\\ 0 & -\dfrac{\gamma}{L}\leqslant\hat{x}\leqslant\dfrac{\gamma}{L}\\ \hat{x}+\dfrac{\gamma}{L} & \hat{x}<-\dfrac{\gamma}{L}\end{cases}\ , \tag{14}$$

here, $\hat{x}$ indicates the result of gradient descent, calculated as follows,

$$\hat{x}=\left(y-\frac{1}{L}\nabla f(y)\right). \tag{15}$$

Here, we can set $x_1=y_0=0^{N\times N}, t_0=1$ as the initial conditions, and end the iteration when $\nabla f(y)$ tends to 0 or the maximum number of iterations has been reached. Note that t is an algorithm parameter used in FISTA and is not related to any practical physical meaning.

After performing the above optimization calculations, we use the continuity of the observed object to perform a Gaussian filtering on the reconstructed image to obtain the final image. Gaussian filtering effectively mitigates the significant differences in structural similarity caused by the sidelobe effect, making the structure of the reconstructed image close to that of the true structure.

As shown in Equation (14), hyperparameter γ represents the compression capability of compressed sensing, and its selection strongly effects the performance of the model. Under different noise conditions, the value of γ must be adjusted so that the compressed sensing algorithm can suppress noise without losing the structure of the original image while retaining a higher PSNR.

3. EXPERIMENTS

3.1. Simulation Scene

One background image with a slowly moving point is given as an example to simulate a quiet sun with a single burst event. In this image, a bright target moves several pixels from the center of the image to the right and down. The image is normalized to $[0,1]$, as shown in Fig. 1. In the remainder of the evaluation, we focus on the center 256 × 256 pixels of the view because the rest of the view is empty.

It is assumed that the image noise is discrete and randomly distributed, and the intensity of the noise will not

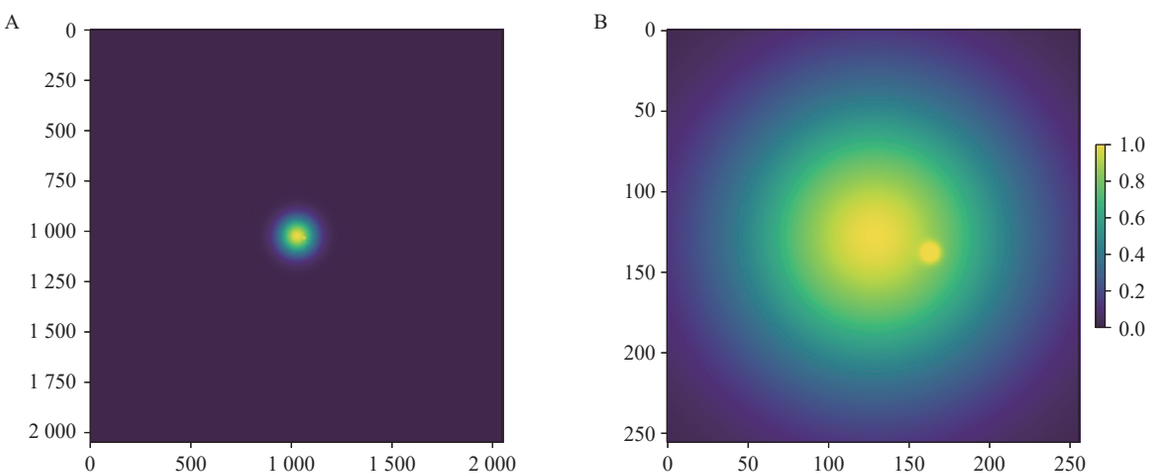

Fig. 1. Observation targets (in pixels). (A) Image of the entire telescope's field of view (2048 × 2048 pixels). (B) The center (256 × 256 pixels).

exceed the intensity of the signal. Therefore, salt-and-pepper noise $N_{\mathrm{s\,\&\,p}}$ was selected for the simulation. Salt-and-pepper noise is predominantly associated with hardware malfunctions. For instance, certain pixel elements within a sensor may become defective, thereby consistently outputting the maximum or minimum grayscale values. During the transmission of image data, the communication channel is susceptible to external electromagnetic interference or signal attenuation, which may introduce errors that set some pixel values to extreme levels. Here, s denotes the intensity of the noise. In this simulation, we set $s = 0.5$. The noisy image I_{noise} is calculated as follows,

$$I_{\mathrm{noise}} = (1-s)I + sN_{\mathrm{s\,\&\,p}}. \tag{16}$$

We denote the density of $N_{\mathrm{s\,\&\,p}}$ as d. The probability distribution of $N_{\mathrm{s\,\&\,p}}$ is given in the following,

$$\begin{cases} p\left(N_{\mathrm{s\,\&\,p}} = I\right) = 1-d, & \text{no noise at this pixel} \\ p\left(N_{\mathrm{s\,\&\,p}} = 1\right) = \dfrac{d}{2}, & \text{salt noise at this pixel} \\ p\left(N_{\mathrm{s\,\&\,p}} = 0\right) = \dfrac{d}{2}, & \text{pepper noise at this pixel} \\ p\left(N_{\mathrm{s\,\&\,p}} = \text{ otherwise }\right) = 0 \end{cases}. \tag{17}$$

This study focuses on the case with known noise densities and standard deviations.

Noised image I_{noise} is shown in Fig 2. Salt-and-pepper noise often occurs because of hardware failures. For example, some pixel units of a sensor may be damaged and always output the highest or lowest gray level values. During the transmission of the image data, the communication channel may be affected by external electromagnetic interference or signal attenuation, and these errors may cause some pixel values to be incorrectly set to extreme values. This study focuses on investigating this type of noise, which is less frequently considered in radio interferometry.

Fig. 2 shows that the noise in the image significantly affects target detection. Because the magnitude of the noise does not exceed the intensity of the targets, the bright targets can still be identified by the signal-to-noise ratio, which provides the possibility of subsequent reconstruction of the image and identification of the targets.

The simulated baseline sampling is presented in Fig. 3. It is dense in the center and sparse around the edges. The minimum baseline is at least 10 times the wavelength, and the maximum baseline is about 1 000 times wavelength. The baseline samples are used to generate a mask vector M. The distribution of these baselines is notably sparse, with only $13\,730 \div 2\,048^2 = 0.33\%$ of the points sampled. In this paper, each pixel represents a wavelength, and hence $\dfrac{\mathrm{pix\_sampled}}{\mathrm{all\_pix}} = \dfrac{N_{\mathrm{sample}}}{\lambda^2}$.

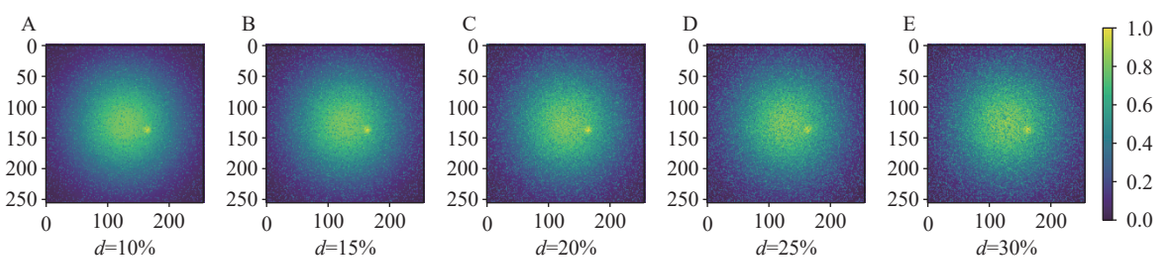

Fig. 2. Observed targets with *d*=10%, 15%, 20%, 25%, 30% (in pixels).

3.2. Image Reconstruction with Different Hyperparameters

We reconstructed the visibility using the FISTA algorithm described above. In the experiments, we set the noise density d to 10%, 15%, 20%, 25% and 30%, and we set hyperparameter $\gamma \in [0.001, 0.1]$ to conduct multi-group experiments. The Fourier transform method was used as a comparison method. For convenient representation, $\gamma = 0$ denotes the Fourier transform. To facilitate the comparison of the signal-to-noise ratio and SSIM of the reconstructed images, the values of the reconstructed the images were scaled to [0, 1].The reconstruction results for different noise densities are shown in Fig. 4A, Fig. 4B, Fig. 4C, Fig. 4D, Fig. 4E. The images of ground truth with different noise density is shown in the last column.

Fig.4A-a, Fig.4B-a, Fig.4C-a, Fig.4D-a, and Fig.4E-a displays the outcomes of the Fourier transformation under varying noise density. As the noise density increases, the clarity of the bright target features in the reconstructed images diminishes, and the signal-to-noise ratio drops. Addi-

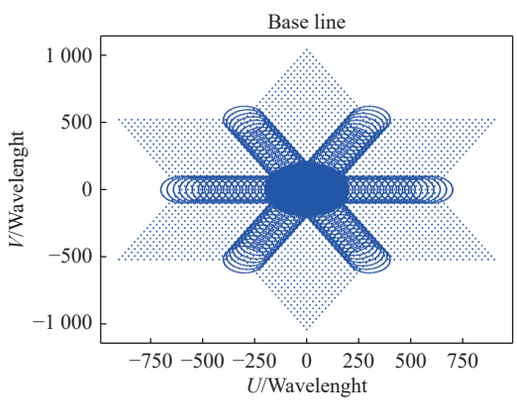

Fig. 3. Spare baselines distribution map (in wavelengths).

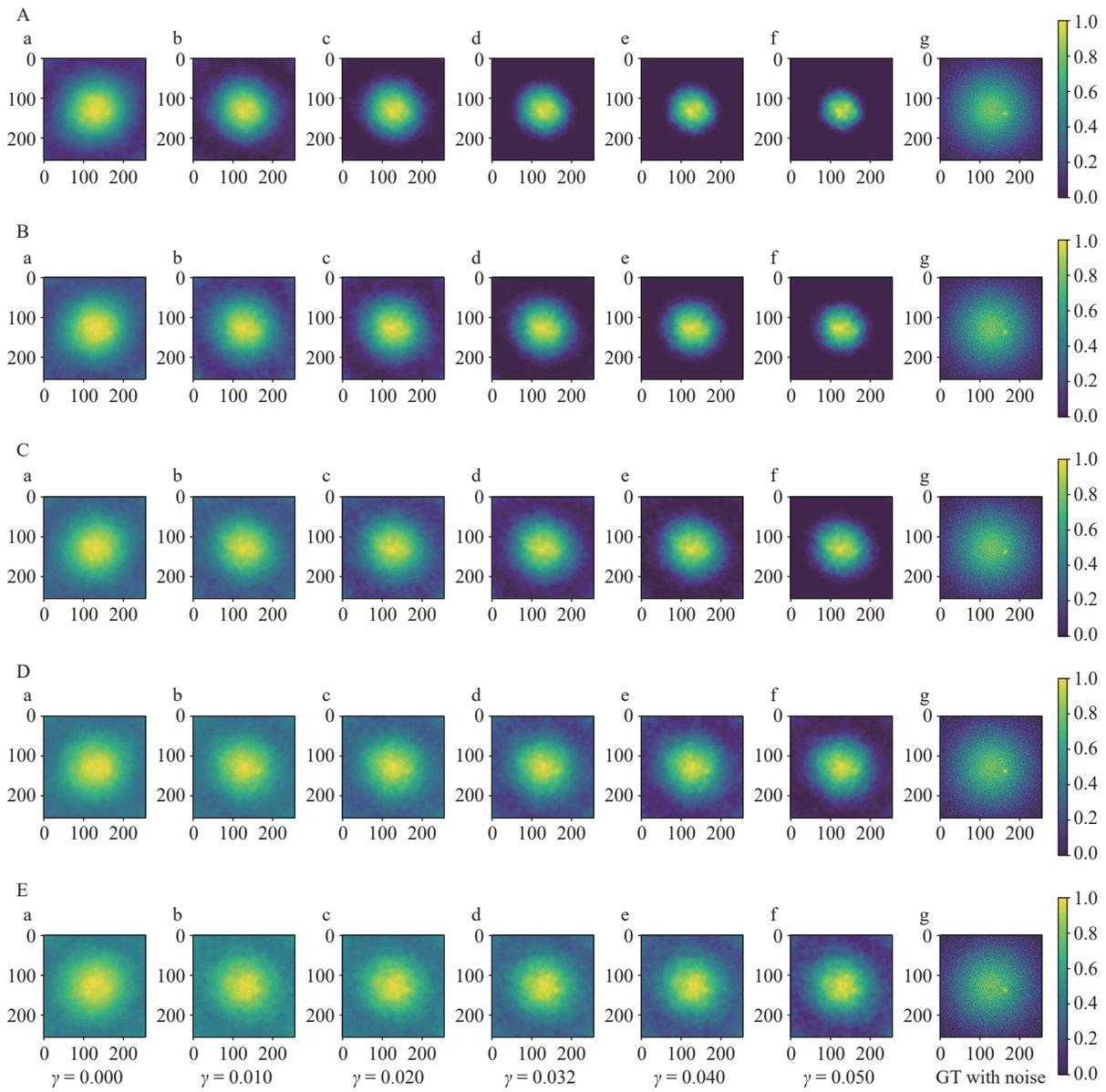

Fig. 4. Reconstruction results for γ=0, 0.01, 0.02, 0.032, 0.04, 0.05 at noise density *d* (column a to f). The last column shows the ground truth with noise. (A) d = 10%; (B) d = 15%; (C) d = 20%; (D) d = 25%; (E) d = 30%.

tionally, the background noise becomes more noticeable. When noise is low, as in Fig.4A-a to Fig.4A-f, increasing γ compresses weaker signals, preserving only the strong ones, which increases this reduction. Fig. 4A-f shows that at $\gamma = 0.05$, only the central 128 × 128 pixel area retains its signal, while the rest of the image is over-regularized to values near zero.

Conversely, when noise density is high, as in Fig. 4E-a to Fig. 4E-f, noise suppression improves with increasing γ. However, even at $\gamma = 0.05$ in Fig. 4E-f, the image has a low signal-to-noise ratio. Comparing Fig. 4A-f and Fig. 4E-f suggests that a high γ over-regularizes the image when noise density is low, but a higher γ is necessary for effective compression when the noise density is high. Comparing Fig. 4A-b, Fig. 4B-c, Fig. 4C-d, Fig. 4D-e, and Fig. 4E-f, better reconstruction is observed when the noise density and hyperparameter γ are well matched. Section 4 provides a quantitative analysis of the reconstruction performance and optimal γ.

4. DISCUSSION

4.1. Reconstruction Performance Under Different Hyperparameter Values

To evaluate the reconstruction performance of sparsely sampled images under noisy conditions, the PSNR and SSIM of the reconstructed images under five levels of noise density and different values of γ were computed. For convenience of notation, γ^*_{PSNR} and γ^*_{SSIM} denote the best γ-values for PSNR and SSIM under the

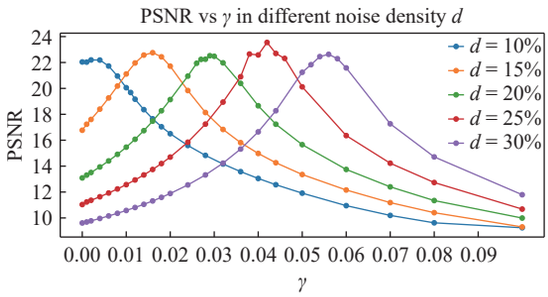

Fig. 5. Variation in PSNR with respect to γ at different noise densities.

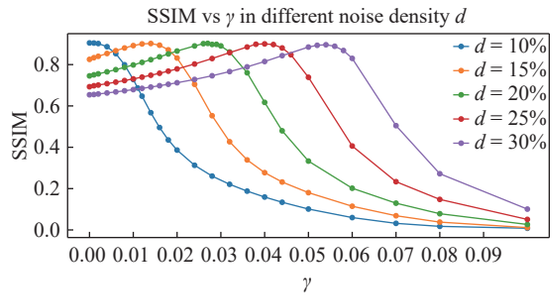

Fig. 6. Variation in SSIM with respect to γ for different noise densities.

given noise conditions. Fig. 5 and Fig. 6 respectively show the variation in the PSNR and SSIM of the reconstructed image with respect to the value of hyperparameter γ.

As Fig. 5 shows, the curves of the PSNR with respect to γ have a single peak. Except for the reconstruction result at noise density $d = 10\%$ which is close to the PSNR of the Fourier transform ($\gamma = 0$ in the figure), as the noise density increases, the PSNR improvement at $\gamma = \gamma^*_{\mathrm{PSNR}}$ increases. As the noise density d increases, similar to the images in Section 3.2, γ^*_{PSNR} increases, and the increases of the PSNR a $\gamma = \gamma^*_{\mathrm{PSNR}}$ become more significant (4–10 dB).

As Fig. 6 shows, when $\gamma < \gamma^*_{\mathrm{SSIM}}$, the curve changes slowly, the image structure is largely retained, only a small amount of edge noise is eliminated, and the similarity is improved by a small amount. By contrast, when $\gamma > \gamma^*_{\mathrm{SSIM}}$, the image structure is severely damaged and the structural similarity decreases dramatically, which is consistent with the reconstruction results in Fig. 4A to Fig. 4C. The selection of γ should try not exceed γ^*_{SSIM}.

Based on the above study, the relationship between the noise density d and γ^*_{PSNR}, γ^*_{SSIM} is further analyzed.

4.2. Relationship Between Noise Density d and Hyperparameter γ

A scatter plot of noise density d and γ^*_{PSNR}, γ^*_{SSIM} is shown in Fig. 7. It can be clearly seen that γ^*_{PSSR} and γ^*_{SSIM} are almost equal and have an approximate linear relationship with the noise density d. Moreover, γ^*_{PSNR} and γ^*_{SSIM} are linearly regressed to d, and the regression equations are given as follows,

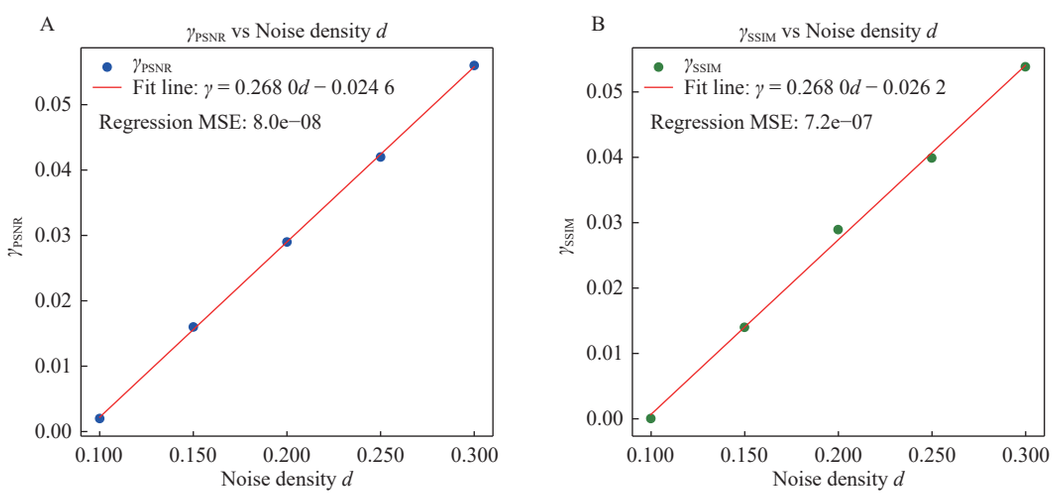

Fig. 7. Percentage of noise versus γ^*_{PSNR} and γ^*_{SSIM}.

$$\gamma^*_{\mathrm{PSNR}} = 0.268d - 0.024\,6, \tag{18}$$

$$\gamma^*_{\mathrm{SSIM}} = 0.268d - 0.026\,2. \tag{19}$$

The equations for the regression (Equation (18) and Equation (19)), reveal that γ^*_{PSNR} and γ^*_{SSIM} have linear regression coefficients that only differ by 0.02 in the constant term. The regression residuals are hence very small. According to the characteristics of γ^*_{SSIM}, when $\gamma < \gamma^*_{\mathrm{SSIM}}$, there is less effect on the structural similarity, and hence we choose $\gamma^* = \gamma^*_{\mathrm{PSNR}}$ as the optimal hyperparameter γ. That is, we set $\gamma^* = 0.268d - 0.024\,6$, and the regression MSE is 8.10×10^{-8}.

5. ROBUSTNESS IN DIFFERENT ANTENNA SCENARIOS

To analyze the scalability of the method, we applied our approach to a variety of different antenna arrays and analyzed the results of the regression. These configura-

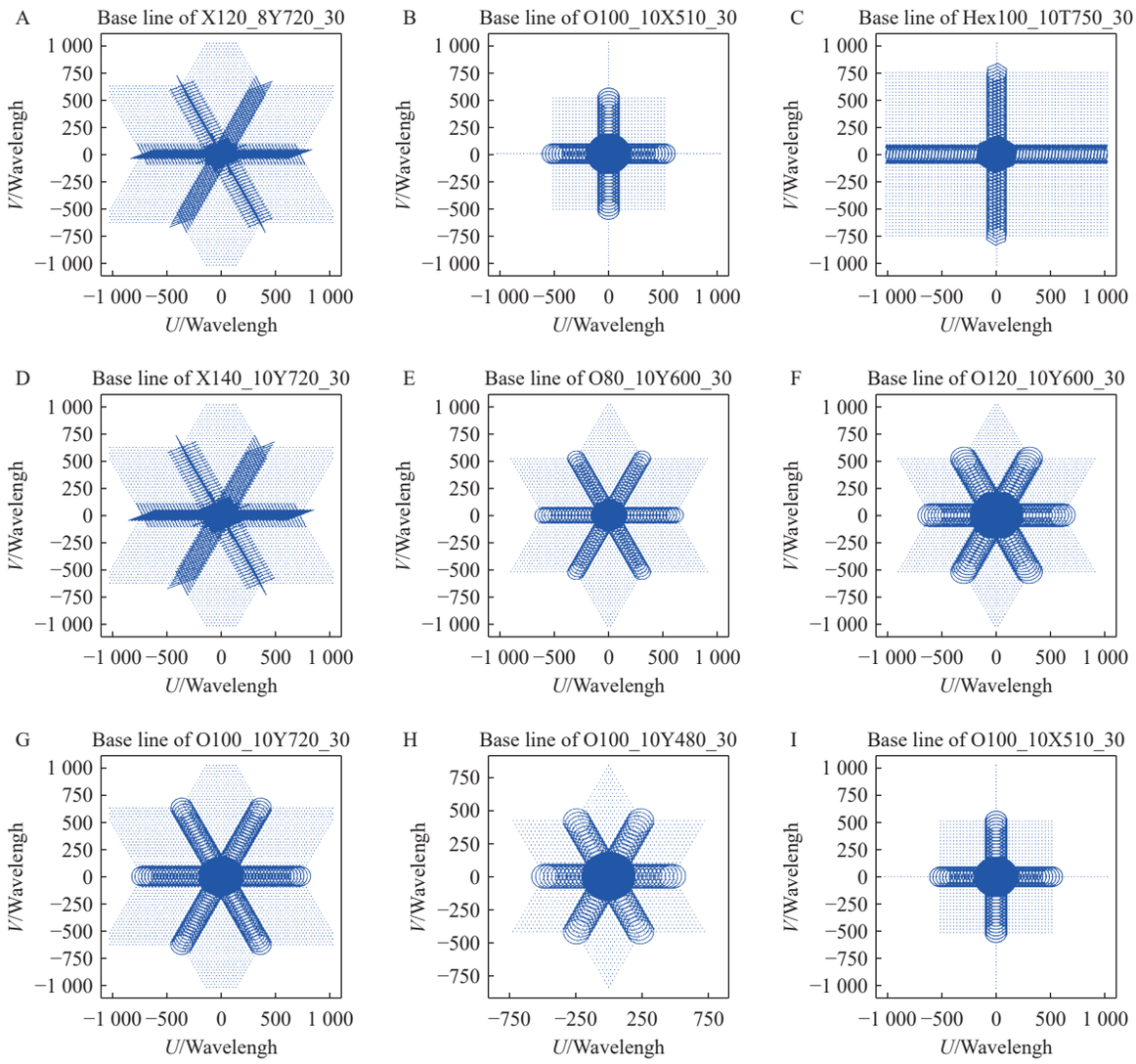

Fig. 8. Baseline results for 9 array configurations.

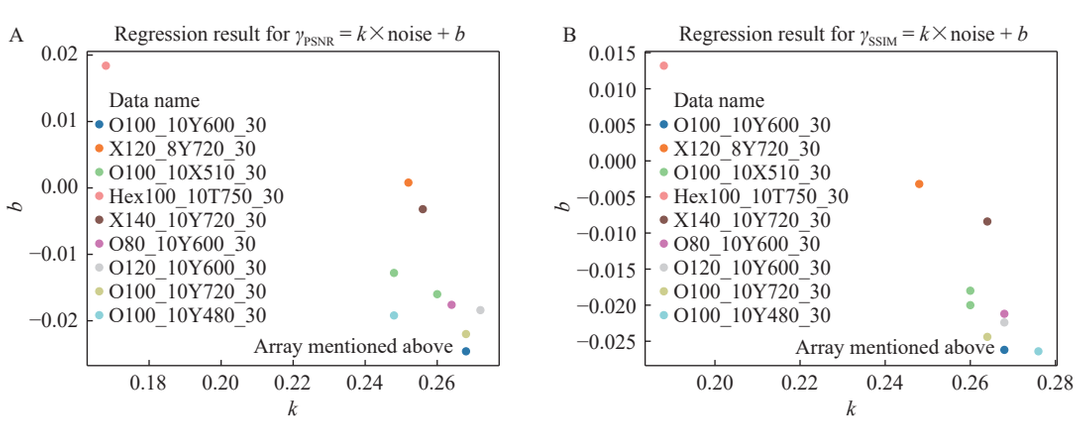

Fig. 9. Regression results for different arrays configurations. The array mentioned above is the array shown in Fig. 3.

tions included various combinations of circular-shaped, cross-shaped, Y-shaped, T-shaped, and hexagonal-shaped arrays, as well as different array sizes. We selected nine arrays for experimentation, and the array sampling numbers and sampling rates are listed in Table 1. The array baseline distribution is shown in Fig. 8. and the experimental results are reported in Fig. 9 and Table 1. Note that the regression result is denoted as $\gamma = kd + b$ for both PSNR and SSIM.

The results of supplementary experiments indicate that for different types of telescope arrays, as long as the minimum antenna spacing is the same and the array is

Table 1. Sampling cases and regression results for 9 antenna configurations

Array name	Samples	Sample rate/(%)	PSNR_k	PSNR_b	SSIM_k	SSIM_b
Array above	13730	0.33	0.268	−0.0246	0.268	−0.0262
X120_8Y720_30	13305	0.32	0.252	0.0008	0.248	−0.0032
O100_10X510_30	13435	0.32	0.26	−0.016	0.26	−0.018
Hex100_10T750_30	11692	0.28	0.168	0.0184	0.188	0.0132
X140_10Y720_30	12625	0.30	0.256	−0.0032	0.264	−0.0084
O80_10Y600_30	11010	0.26	0.264	−0.0176	0.268	−0.0212
O120_10Y600_30	16997	0.41	0.272	−0.0184	0.268	−0.0224
O100_10Y720_30	16295	0.39	0.268	−0.022	0.264	−0.0244
O100_10Y480_30	11433	0.27	0.248	−0.0192	0.276	−0.0264
O100_10X510_30	13435	0.32	0.248	−0.0128	0.26	−0.02

quasi-symmetric (e.g., Y-shaped, cross-shaped, or circular-shaped arrays with approximately equal distributions in the U and V directions), the slope of the regression results exhibits good robustness, yielding a slope for the linear fitting results of 0.26 ± 5%. However, when the minimum antenna spacing changes or there is a significant bias in the baseline distribution (e.g., Hex100_10T750_30), the robustness of the results changes substantially.

6. CONCLUSION

In this paper, we analyzed the effect of noise density d and hyperparameter γ on the reconstruction performance of compressed sensing algorithm during interferometric imaging image reconstruction. We chose images with salt-and-pepper noise as our simulation inputs. The results show that when the noise density d is constant, if γ is too small, the image cannot be effectively denoised, and if it is too large, the image structure may be seriously affected. Hence, it is very important to choose a suitable value for γ. Under the conditions of noise density $d = 10\% - 30\%$, when the optimal value of γ is selected, the compressed sensing method can improve the PSNR by 6–10 dB, and substantially improve the retention of image structure, increasing the SSIM to about 0.9. The optimal hyperparameter γ^* has a linear relationship with noise density d, this is $\gamma^*_{\mathrm{PSNR}} = 0.268d - 0.024\,6$. Moreover, the regression MSE is 8.10×10^{-8}. The noise type, noise intensity, and characteristics are important factors affecting the selection of γ, and further research on these factors should be carried out.

AI DISCLOSURE STATEMENT

Deepl and Kimi was employed for language and grammar checks within the article. The authors carefully reviewed, edited, and revised the Deepl and Kimi-generated texts to their own preferences, assuming ultimate responsibility for the content of the publication.

AUTHOR CONTRIBUTIONS

Haoming Dai conceived the ideas, implemented the study, and wrote the paper. Li Deng supervised this paper. All authors read and approved the final manuscript.

DECLARATION OF INTERESTS

The authors declare no competing interests.

REFERENCES

[1] Candes, E. J., Romberg, J., Tao, T. 2006. Robust uncertainty principles: exact signal reconstruction from highly incomplete frequency information. *IEEE Transactions on Information Theory*, **52**(2): 489−509.

[2] Candes, E. J., Tao, T. 2006. Near-optimal signal recovery from random projections: Universal encoding strategies? *IEEE Transactions on Information Theory*, **52**(12): 5406−5425.

[3] Donoho, D. 2006. Compressed sensing. *IEEE Transactions on Information Theory*, **52**(4): 1289−1306.

[4] Elad, M., Aharon, M. 2006. Image denoising via sparse and redundant representations over learned dictionaries. *IEEE Transactions on Image Processing*, **15**(12): 3736−3745.

[5] Yang, C. L., Shen, J. L., Peng, J. Y., et al. 2013. Image collection summarization via dictionary learning for sparse representation. *Pattern Recognition*, **46**(3): 948−961.

[6] Peyre, G. 2010. Best basis compressed sensing. *IEEE Transactions on Signal Processing*, **58**(5): 2613−2622.

[7] Shahdoosti, H. R., Hazavei, S. M. 2019. A new compressive sensing based image denoising method using block-matching and sparse representations over learned dictionaries. *Multimedia Tools and Applications*, **78**(9): 12561−12582.

[8] Bobin, J., Starck, J. L., Ottensamer, R. 2008. Compressed sensing in astronomy. *IEEE Journal of Selected Topics in Signal Processing*, **2**(5): 718−726.

[9] Wenger, S., Rau, U., Magnor, M. 2013. A group sparsity imaging algorithm for transient radio sources. *Astronomy and Computing*, **1**: 40−45.

[10] Beck, A., Teboulle, M. 2009. A fast iterative shrinkage-thresholding algorithm for linear inverse problems. *SIAM Journal on Imaging Sciences*, **2**(1): 183−202.

[11] Bioucas-Dias, J., Figueiredo, M. 2007. A new TwIST: Two-step iterative shrinkage/thresholding algorithms for image restoration. *IEEE Transactions on Image Processing*, **16**(12): 2992−3004.